

Thermodynamic properties and structural stability of thorium dioxide

Yong Lu,¹ Yu Yang,¹ and Ping Zhang^{1,2,*}

¹*LCP, Institute of Applied Physics and Computational Mathematics, Beijing 100088, China*

²*Center for Applied Physics and Technology, Peking University, Beijing 100871, China*

(Dated: November 27, 2024)

Using density functional theory (DFT) calculations, we have systematically investigated the thermodynamic properties and structural stabilities of thorium dioxide (ThO₂). Based on the calculated phonon dispersion curves, we calculate the thermal expansion coefficient, bulk modulus, and heat capacities at different temperatures for ThO₂ under the quasi-harmonic approximation. All the results are in good agreement with corresponding experiments proving the validity of our methods. Our theoretical studies can help people more clearly understand the thermodynamic behaviors of ThO₂ at different temperatures. In addition, we have also studied possible defect formations and diffusion behaviors of helium in ThO₂, to discuss its structural stability. It is found that in intrinsic ThO₂ without any Fermi energy shifts, the interstitial Th_i⁴⁺ defect other than oxygen or thorium vacancies, interstitial oxygen, and any kinds of Frenkel pairs, is most probable to form with an energy release of 1.74 eV. However, after upshifting the Fermi energy, the formation of the other defects also becomes possible. For helium diffusion, we find that only through the thorium vacancy can it happen with the small energy barrier of 0.52 eV. Otherwise, helium atoms can hardly incorporate or diffuse in ThO₂. Our results indicate that people should prevent upshifts of the Fermi energy of ThO₂ to avoid the formation of thorium vacancies and so as to prevent helium caused damages.

PACS numbers: 63.20.dk, 65.40.-b, 61.72.-y, 66.30.J-.

I. INTRODUCTION

As the world's demands for energy keep growing, corresponding researches on developing new energy sources or enhancing the energy-consuming efficiency are attracting more and more attentions. Until now, the fissile nuclear reactor is still a very important energy source, in which uranium dioxide (UO₂) has been the main fuel component for many years [1–5]. However, during the burning cycle of UO₂, considerable amounts of radioactive elements emerge in the reaction waste [6]. And such radioactive waste results in very troublesome long-term storage requirements. Based on these facts, many efforts have been done to look for possible substitutions of UO₂. Thorium based materials, which are naturally abundant, are identified as good candidates for replacing UO₂ in fissile nuclear reactors because they are able to produce fewer transuranic (TRU) compared to uranium- and plutonium-based fuels. And although ²³³Th is not fissile, it can absorb a slow neutron and then form fissile ²³³U just undergoing multiple beta-decays [7]. Moreover, because of the good solubility between thorium dioxide (ThO₂) and other transuranic dioxides, using the mix oxides (MOX) of thorium and plutonium in nuclear reactors can also help reducing the large plutonium stockpile while maintaining acceptable safety and control characteristics of the reactor system [8]. In comparison with previous uranium-based fuels, the thorium-based fuels also have many additional physical advantages, such as

higher melting points, higher corrosion resistivity, lower thermal expansion coefficients, and higher thermal conductivity [9]. In recent years, the thorium-based fuels have already been tested in different reactors [7, 10–12].

As in the front position of actinide element, thorium and its compounds have been studied ever since 1950. At the earliest stage, a series of experimental measurements have been carried out on the thermal properties of ThO₂ such as the thermal expansion coefficient, heat capacity, and thermal conductivity [13–22]. In 1997, Bakker *et al.* [23] presented a conclusion and comparison for the measured values. On the other side, Chadwick and Graham [24], Allen and Tucker [25], and Veal *et al.* [26] investigated the valence-band structures of thorium and its oxides by means of X-ray photoemission spectroscopy. And the pressure-induced phase transition of ThO₂ has been studied by Jayaraman [27], Dancausse [28], and Idiri [29] *et al.* experimentally. Recently in 2006, researchers from the international atomic energy agency (IAEA) built a thermal-physical database of materials for light water reactors and heavy water reactors [30]. And the earlier experimental measurements are re-addressed.

Despite the vast experimental measurements, it is to our surprise that no one has ever theoretically investigated the thermodynamic properties and defect behaviors for ThO₂, which are critically important for its usage in thermonuclear reactors. Only recently, several theoretical studies have been carried out on the mechanical and electronic properties [31–33], phase transition behaviors [34, 35], and elastic and optical properties [36] for ThO₂. Our previous study has already proven that the thorium *5f* states is no longer localized after electronic hybridizations, and density functional theory calculations are enough to produce correct descriptions for

*Author to whom correspondence should be addressed. E-mail: zhang_ping@iapcm.ac.cn

the ground-state properties of ThO₂ [35]. So in our present paper, we decide to systematically investigate the thermodynamic properties and structural stabilities of ThO₂, by using density functional theory calculations. The thermodynamic stability will be discussed based on the calculated thermal parameters, while the structural stability will be discussed by calculating the formation energy of different kinds of defects, and diffusion energy barriers of helium in ThO₂. The rest of the paper is organized as follows. The computation methods are introduced in Section II. The discussions about the thermodynamic properties and structural stabilities of ThO₂ are presented in Section III. Finally, we give our conclusions in Section IV.

II. CALCULATION METHODS

The density functional theory (DFT) calculations are carried out using the Vienna *ab initio* simulations package (VASP) [37, 38] with the projector-augmented-wave (PAW) potential methods [39]. The cutoff energy for the plane-wave basis set is set to 500 eV. The exchange and correlation effects are described by generalized gradient approximation (GGA) in the Perdew-Burke-Ernzerhof (PBE) form [40]. A 2×2×2 supercell is employed to study defect formation and helium diffusions inside ThO₂. For calculations of the unit cell (12 total atoms) and 2×2×2 supercell (96 total atoms), the integration over the Brillouin Zone is done on 13×13×13 and 5×5×5 *k*-point meshes generated using the Monkhorst-Pack [41] method, which are both proven to be sufficient for energy convergence of less than 1.0×10⁻⁴ eV per atom. During the supercell calculations, the shape and size of the supercell are fixed while all the ions are free to relax until the forces on them are less than 0.01 eV/Å.

For a semiconductor, the Helmholtz free energy F at volume V and temperature T can be expressed as

$$F(V, T) = E(V) + F_{vib}(V, T), \quad (1)$$

where $E(V)$ stands for the ground-state electronic energy, $F_{vib}(V, T)$ is the phonon free energy at a given unit cell volume V . Within quasi-harmonic approximation (QHA), $F_{vib}(V, T)$ can be evaluated by

$$F_{vib}(V, T) = k_B T \sum_{j, \mathbf{q}} \ln \left[2 \sinh \left(\frac{\hbar \omega_j(\mathbf{q}, V)}{2k_B T} \right) \right], \quad (2)$$

where $\omega_j(\mathbf{q}, V)$ is the phonon frequency of the j th phonon mode with wave vector \mathbf{q} at fixed V , and k_B is the Boltzmann constant. The total specific heat of the crystal is the sum of all phonon modes over the Brillouin zone (BZ),

$$C_v(T) = \sum_{j, \mathbf{q}} c_{v,j}(\mathbf{q}, T). \quad (3)$$

$c_{v,j}(\mathbf{q}, T)$ is the mode contribution to the specific heat

defined as,

$$c_{v,j}(\mathbf{q}, T) = k_B \sum_{j, \mathbf{q}} \left(\frac{\hbar \omega_j(\mathbf{q}, V)}{2k_B T} \right)^2 \frac{1}{\sinh^2[\hbar \omega_j(\mathbf{q}, V)/2k_B T]}. \quad (4)$$

The mode Grüneisen parameter $\gamma_j(\mathbf{q})$ describing the phonon frequency shift with respect to the volume can be calculated by

$$\gamma_j(\mathbf{q}) = -\frac{d[\ln \omega_j(\mathbf{q}, V)]}{d[\ln V]}. \quad (5)$$

The acoustic Grüneisen parameter $\gamma(T)$ defined as the weighted average of the mode Grüneisen parameters for all acoustic phonon branches is calculated to be

$$\gamma(T) = \frac{\alpha_v(T)B(T)V_m(T)}{C_v(T)}, \quad (6)$$

where $\alpha_v(T)$ is the thermal expansion coefficient and equals to $\frac{1}{V} \left(\frac{\partial V}{\partial T} \right)_P$, $V_m(T)$ is the volume per mole material, and $B(T)$ and $C_v(T)$ are the bulk modulus and specific heat respectively.

The formation energy of a point defect X with charges q can be calculated by introducing the chemical potential concept as,

$$E_{for}(X^q) = E_{tot} \pm n_x \mu - E_{\text{ThO}_2} + q(E_v + E_f + \Delta V), \quad (7)$$

where E_{tot} is the total energies of the supercell with defect X, n_x represents the number of X defects, μ is the chemical potential of X with a positive sign for vacancy and a negative sign for interstitial defect, E_{ThO_2} is the energy of the ThO₂ supercell without defects, E_v and E_f are the valence-band maximum (VBM) and the Fermi level of ThO₂ respectively. With these denotations, $E_{for}(\text{V}_O^0)$, $E_{for}(\text{O}_i^0)$, $E_{for}(\text{V}_{\text{Th}}^0)$, and $E_{for}(\text{Th}_i^0)$ represent for the formation energies of a neutral oxygen vacancy, a neutral interstitial oxygen, a neutral thorium vacancy, and a neutral interstitial thorium respectively. The shift of the VBM in a defect supercell ΔV takes the change of the valence-band maximum caused by the defect into account. Its value can be obtained by a macroscopic average technique [42, 43] through calculating the difference between the average electrostatic potential in a bulklike environment of the defect supercell and the average electrostatic potential in the defect-free supercell. The formation energy of a Frenkel-pair can be calculated by summing up the formation energies of a vacancy and a corresponding interstitial add-in, i.e.,

$$E_{for}(\text{FP}_X) = E_{for}(\text{V}_X) + E_{for}(\text{X}_i). \quad (8)$$

For the Schottky defect, the formation energy can be calculated by

$$E_{for}(\text{S}) = E_{for}(\text{V}_{\text{Th}}) + 2E_{for}(\text{V}_O) - \frac{3(N-1)}{N} E_{\text{ThO}_2}, \quad (9)$$

where N is the number of atoms in the considered supercell. In this expression, the defect consists of a thorium vacancy and two oxygen vacancies, which are again supposed to be non-interacting.

III. RESULTS AND DISCUSSIONS

A. Structure and Elastic constants of ThO₂

Our previous studies have shown that DFT calculations with GGA exchange-correlation functionals are good enough for obtaining the ground-state properties of ThO₂ [47], and adding additional U or J modifications for localization effects might lead to incorrect results. We believe that it is because the 5*f* electronic states of Th become delocalized after electronic hybridizations in ThO₂. Here based on our previous studies, we further investigate the thermodynamic properties of ThO₂.

From the mechanical point of view, the theoretical equilibrium volume V_0 , bulk modulus B_0 , and the pressure derivative of bulk modulus B' can be obtained by fitting the third-order Birch-Murnaghan equation of state [44]. In this way, our calculated lattice parameter a_0 for ThO₂ is 5.619 Å, which is in accordance with the experimental data of 5.60 Å [29, 45]. The bulk modulus B_0 and its pressure derivative B' are calculated to be 190 GPa and 4.3, also in agreement with corresponding experimental values of 195-198 GPa and 4.6-5.4 [29, 45], respectively. In order to evaluate the Poisson's ratio ν , we calculated the three independent elastic constants C_{11} , C_{12} and C_{44} of ThO₂. The calculation methods are the same as in our previous studies [35, 46, 47]. The obtained elastic constants for ThO₂ are C_{11} =351.2 GPa, C_{12} =106.9 GPa, and C_{44} =74.1 GPa, which are in accordance with experimentally measured values of C_{11} =367 GPa, C_{12} =106 GPa, and C_{44} =79 GPa [48]. Furthermore, the Poisson's ratio ν is calculated to be 0.293, in excellent accordance with the experimental data of 0.285 [48]. All the good agreement between our calculated values and corresponding experimental measurements indicates that our calculation methods are effective and reliable. In comparison with other actinide dioxides, we can see that ThO₂ has a slightly smaller bulk modulus than UO₂ and PuO₂ [47].

B. Phonon dispersions, Thermal expansion, and Heat capacity of ThO₂

The thermodynamic properties of a material are connected to its phonon dispersion curves. In order to get accurate splittings between longitudinal (LO) and transverse optical (TO) phonon branches, the Born effective charge is firstly calculated. Because of the high symmetry of ThO₂, the Born transverse effective charge tensor \mathbf{Z}^* is the same along the [100], [010], and [001] directions, and the effective charge can be averaged by $Z^* = \frac{1}{3}Tr\mathbf{Z}^*$. For ThO₂, we obtain that $Z_{Th}^* = +5.41$, and $Z_O^* = -2.71$. The static dielectric constant $\epsilon = \frac{1}{3}Tr\epsilon$ is 4.83. The dielectric constant might be smaller than experimental measurements because of the underestimation of the electronic energy band gap due to the drawback of the exchange-correlation approximation (GGA).

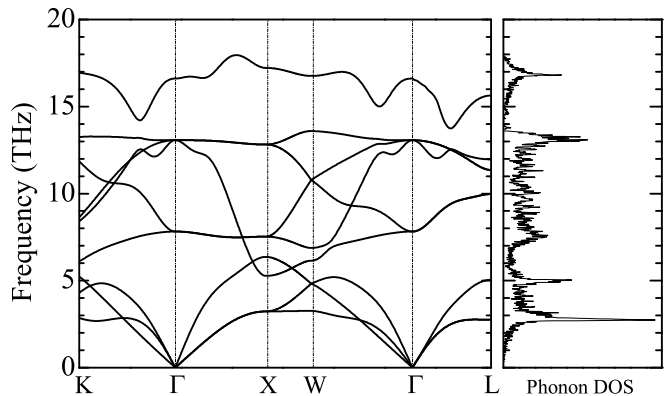


FIG. 1: (Color online) Phonon dispersion curves and phonon density of states (DOS) for ThO₂.

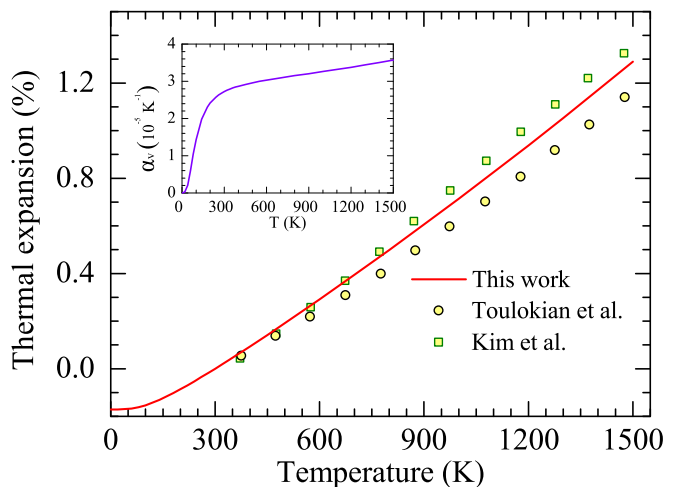


FIG. 2: (Color online) Temperature dependence of the linear thermal expansion for ThO₂. The inset is the volume thermal expansion coefficient as a function of temperature.

The calculated phonon dispersion curves along the high-symmetry k-point lines using the above Born effective charges are shown in Fig. 1. As clearly shown, there is an obvious splitting between longitudinal optical (LO) and TO branches due to the Born effective charge. Moreover, we find that there is no evident gap between acoustic and optical branches of phonon for ThO₂, with an observable overlap between the longitudinal acoustic (LA) and transverse optical (TO) branches around the X point. Detailed vibrational modes analysis tells us that the vibrations of Th and O atoms dominate the low- (0-6 THz) and high-frequency (6-18 THz) modes, respectively.

From the obtained phonon dispersion curves and Eqs. (1) and (2), we then calculate the energy curves for ThO₂, and find the lowest-energy lattice constants at different temperatures. The lattice expansion curve is thus obtained and shown in Fig. 2. The experimental data by Touloukian *et al.* [49] and Kim *et al.* [30] are also shown

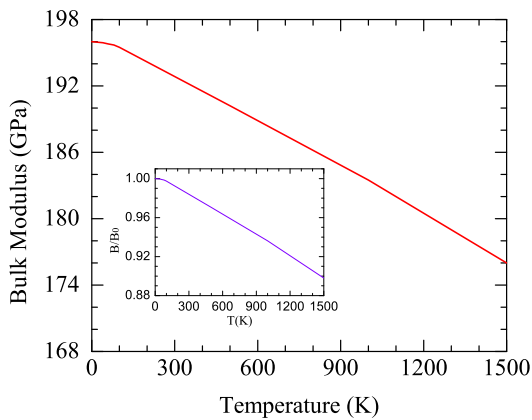


FIG. 3: (Color online) Temperature dependence of bulk modulus B for ThO_2 . The inset is the ratio of B/B_0 .

in Fig. 2 for comparisons with our calculational results. One can see that in the temperature range from 300 to 600 K, our result is in excellent agreement with the experimental data. In a higher temperature range from 600 to 1500 K, our obtained theoretical values are in the middle of the two different experimental measurements. And at 1500 K, the relative difference between our result and the two experimental values are 0.15% and 0.05%, respectively. The small relative differences indicate that the QHA method can give reasonable lattice parameters for ThO_2 up to 1500 K. The thermal expansion coefficient $\alpha_v(T)$ is calculated and shown in the inset of Fig. 2. The experimental values for the thermal expansion coefficient in the temperature range from 298 to 1500 K can be calculated from the corresponding thermal expansion curves, which are $3.318 \times 10^{-5} \text{K}^{-1}$ for Touloukian's data and $3.630 \times 10^{-5} \text{K}^{-1}$ for Kim's data, respectively. Our theoretical result of $3.509 \times 10^{-5} \text{K}^{-1}$ is consistent with the experimental values.

The bulk modulus B is also analyzed as a function of temperature according to the formula $B = V_0(\frac{\partial^2 F}{\partial V^2})_{V_0}$, and the result is displayed in Fig. 3. We can see that the value of bulk modulus decreases with increasing temperature, and at 1500 K, the ratio of bulk modulus (B/B_0) is 0.898, as depicted in the inset of Fig. 3.

Under QHA, the considered vibration modes are harmonic but volume-dependent. The calculated heat capacity at constant volume using Eqs. (3) and (4) is shown in Fig. 4, together with the heat capacity at constant pressure C_p , which is calculated according to the relationship,

$$C_p - C_v = \alpha_v^2(T)B(T)V(T)T. \quad (10)$$

The available experimental data from Bakker *et al.* [23] and Kim *et al.* [30] are also shown in Fig. 4 for comparisons. It is evident that our theoretical result is in excellent agreement with the measured values for the whole experimentally considered temperature range. As temperature increases, the value of C_p increases continuously,

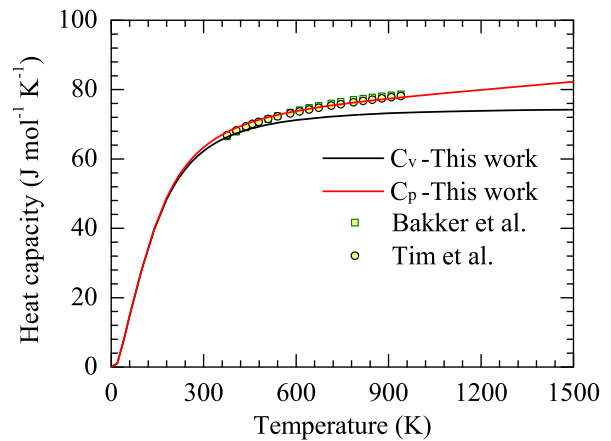


FIG. 4: (Color online) Heat capacities at constant volume (C_v) and constant pressure (C_p) of ThO_2 .

while the value of C_v approaches to a constant of $3R$ (R is the Rydberg constant). At 1500 K, the value of C_p becomes $81 \text{ J} \cdot \text{mol}^{-1} \text{K}^{-1}$. In general, QHA method is valid when the temperature is much lower than the material's melting point (around 3600 K for ThO_2 [23]) when the anharmonic effect is small.

C. Grüneisen parameters and thermal conductivity of ThO_2

The lattice thermal conductivity κ_L for a material can be calculated differently, depending on the specific mechanisms for phonon scattering. At relative high temperatures, the dominant mechanism for phonon scattering is the Umklapp process, in which the acoustic phonon branches interact with each other and transport heat. With this mechanism, the lattice thermal conductivity of a crystal-like material can be expressed as [50–52],

$$\kappa_L = A \frac{\bar{M} \Theta^3(T) \delta(T) n^{2/3}}{\gamma^2(T) \times T}, \quad (11)$$

where A is a physical constant with the value of 3.1×10^{-6} , \bar{M} is the average mass per atom in the crystal, $\Theta(T)$ is the Debye temperature of ThO_2 , n is the number of atoms in the primitive unit cell, $\gamma(T)$ is the acoustic Grüneisen parameter, and $\delta(T)$ is the cube root of the average volume per atom, i.e., the averaged radius per atom. The κ_L and δ in Eq. (11) are in units of $\text{W m}^{-1} \text{K}^{-1}$, and \AA respectively. With reasonable expressions of the Debye temperature and acoustic Grüneisen parameter to describe the harmonic phonon branches and the anharmonic interactions between different phonon branches, Eq. (11) can provide accurate predictions for a material's thermal conductivity [51].

Firstly the Debye temperature Θ can be determined from the elastic constants within the Debye theory, in which the vibrations of the solid are considered as elastic

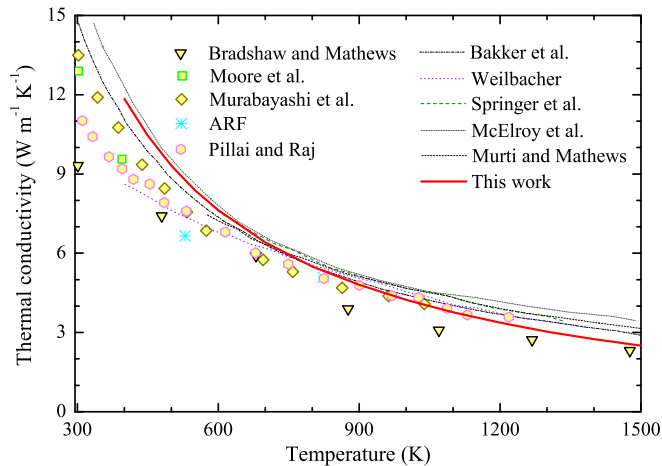


FIG. 5: (Color online) The thermal conductivity of ThO_2 . Experimental results from Springer *et al.* [14], Weibacher [15], McElroy *et al.* [16], ARF [17], Murabayashi *et al.* [18], Pillai and Raj [19], Bradshaw [20], Moore *et al.* [21], Murti and Mathews [22], and Bakker *et al.* [23] are displayed for comparison.

waves, and the Debye temperature of the solid is related to an averaged sound velocity [53]. Within isotropic approximation, the Debye temperature Θ can be expressed as [53],

$$\Theta(T) = \frac{\hbar}{k_B} [6\pi^2 V^{1/2}(T)n]^{1/3} f(\nu) \sqrt{\frac{B(T)}{M}}, \quad (12)$$

where M is the molecular mass per formula unit, $B(T)$ is the bulk modulus, ν is the material's Poisson's ratio, and $f(\nu)$ is given by [54, 55]

$$f(\nu) = 3^{1/3} \left[2 \left(\frac{2}{3} \frac{1+\nu}{1-2\nu} \right)^{3/2} + \left(\frac{1}{3} \frac{1+\nu}{1-\nu} \right)^{3/2} \right]^{-1/3}. \quad (13)$$

Our calculations find that the Debye temperature monotonically decreases, while the acoustic Grüneisen parameter monotonically increases with increasing temperature.

Based on Eq. (11) and the obtained Debye temperature, we calculate the thermal conductivity for ThO_2 . Figure 5 shows our thermal conductivity result, in comparison with the previous experimental measurements in the temperature range from 300 to 1500 K. We can see that in the considered temperature range, our calculated values are in agreement with the experimental results, which proves the validity of our methods and model. Especially, in the high temperature range from 600 to 1200 K, our results accords very well with the experimental measurements by Murabayashi, *et al.* [18] and by Pillai and Raj [19]. At the low temperature range around the Debye temperature of 402 K, our results are slightly different from some experimental results. This difference comes from our presumption that the dominant mechanism for phonon scattering is the Umklapp process. The

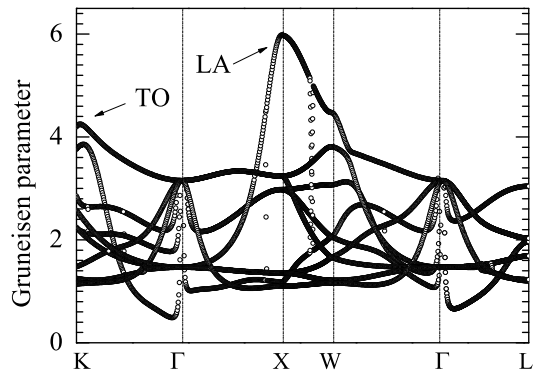


FIG. 6: (Color online) The mode Grüneisen parameters along high-symmetry directions in the reciprocal lattice space of ThO_2 .

accordance between our calculations and corresponding experiments in the temperature range from 600 to 1200 K proves that within this temperature area, the contributions from other phonon-scattering mechanisms are so small that can be neglected.

The mode Grüneisen parameter describing the phonon frequency shift with respect to the volume can be used to discuss the anharmonic effects. By expanding or compressing the equilibrium volume by 1%, we calculate the mode Grüneisen parameter $\gamma_j(\mathbf{q})$ for all nine phonon branches according to Eq. (5). The corresponding results are shown in Fig. 6. It can be seen that all the mode Grüneisen parameter values are positive, indicating that all phonon frequencies increase with decreasing volume. Besides, the acoustic phonon mode Grüneisen parameters are relatively larger reflecting that changes in volume have more influences on the collective vibration modes of ThO_2 . We can also see from Fig. 6 that the LA and TO phonon branches have larger mode Grüneisen parameters, indicating that the anharmonic interactions between the LA and TO branches should be more intensive with respect to the volume change.

D. Defect formation in ThO_2

In this subsection and the next, we will investigate the structural stability of ThO_2 by systematically calculating the formation energy of different kinds of defects and investigating the diffusion behaviors of helium. A $2 \times 2 \times 2$ supercell with 96 Th and O atoms is employed in these two subsections to model defect formation and helium diffusion in ThO_2 . Different charge states are considered for all the defects. To calculate the formation energy, the positions of all ions are fully relaxed before we calculate the electronic free energies of the system with different defects.

The formation energy for oxygen (thorium) vacancies, interstitial oxygen (thorium) ions, oxygen (thorium) Frenkel pairs, and the Schottky defect of a ThO_2 unit in

TABLE I: Formation energies of different defects at different charge states in ThO_2 . The defects include oxygen vacancy (V_{O}), interstitial oxygen ion (O_i), thorium vacancy (V_{Th}), interstitial thorium ion (Th_i), oxygen (FP_{O}) and thorium Frenkel-pairs (FP_{Th}), and Schottky defect (S) of a ThO_2 unit. The formation energies are in units of eV.

Defect	Charge on defect	Kröger-Vink notation	E_{for}
V_{O}	0	V_{O}^{\times}	7.415
V_{O}	+1	V_{O}^{\bullet}	3.922
V_{O}	+2	$V_{\text{O}}^{\bullet\bullet}$	1.338
O_i	0	O_i^{\times}	1.901
O_i	-1	O_i^{\prime}	4.026
O_i	-2	$O_i^{\prime\prime}$	5.487
V_{Th}	0	V_{Th}^{\times}	18.349
V_{Th}	-1	V_{Th}^{\prime}	18.600
V_{Th}	-2	$V_{\text{Th}}^{\prime\prime}$	18.314
V_{Th}	-3	$V_{\text{Th}}^{\prime\prime\prime}$	18.327
V_{Th}	-4	$V_{\text{Th}}^{\prime\prime\prime\prime}$	18.462
Th_i	0	Th_i^{\times}	6.094
Th_i	+1	Th_i^{\bullet}	5.897
Th_i	+2	$\text{Th}_i^{\bullet\bullet}$	2.869
Th_i	+3	$\text{Th}_i^{\bullet\bullet\bullet}$	0.488
Th_i	+4	$\text{Th}_i^{\bullet\bullet\bullet\bullet}$	-1.741
FP_{O}	0	$V_{\text{O}}^{\times} + O_i^{\times}$	9.316
FP_{O}	0	$V_{\text{O}}^{\bullet} + O_i^{\prime}$	7.948
FP_{O}	0	$V_{\text{O}}^{\bullet\bullet} + O_i^{\prime\prime}$	6.825
FP_{Th}	0	$V_{\text{Th}}^{\times} + \text{Th}_i^{\times}$	24.443
FP_{Th}	0	$V_{\text{Th}}^{\prime} + \text{Th}_i^{\bullet}$	24.497
FP_{Th}	0	$V_{\text{Th}}^{\prime\prime} + \text{Th}_i^{\bullet\bullet}$	21.183
FP_{Th}	0	$V_{\text{Th}}^{\prime\prime\prime} + \text{Th}_i^{\bullet\bullet\bullet}$	18.815
FP_{Th}	0	$V_{\text{Th}}^{\prime\prime\prime\prime} + \text{Th}_i^{\bullet\bullet\bullet\bullet}$	16.721
S	0	$V_{\text{Th}}^{\times} + 2V_{\text{O}}^{\times}$	19.472
S	0	$V_{\text{Th}}^{\prime} + 2V_{\text{O}}^{\bullet}$	12.651
S	0	$V_{\text{Th}}^{\prime\prime} + 2V_{\text{O}}^{\bullet\bullet}$	8.231

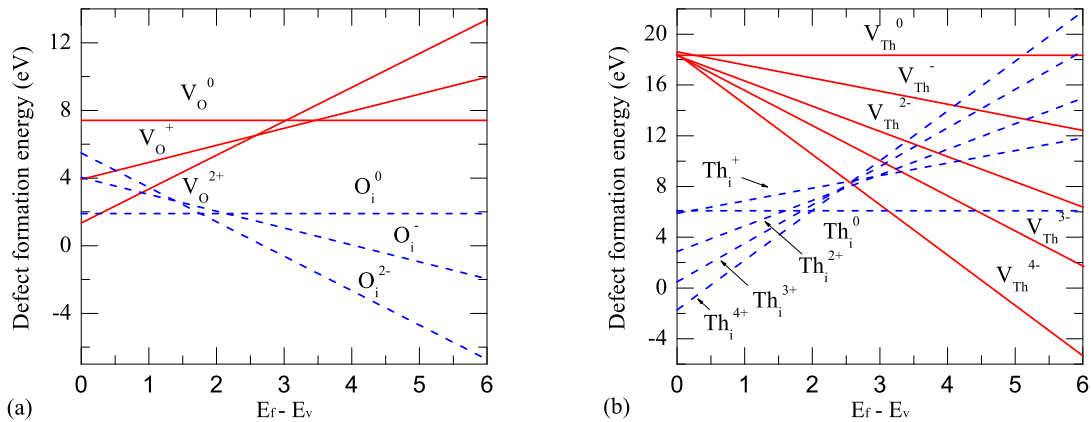


FIG. 7: (Color online) Formation energies of oxygen related defects, i.e., oxygen vacancies or interstitial oxygen ions (a) and thorium related defects, i.e., thorium vacancies or interstitial thorium ions (b) as functions of the Fermi energy.

the $2 \times 2 \times 2$ supercell are obtained and listed in Table I. One can see that the charged Th_i^{4+} add-in defect is the only one having a negative formation energy. It means that once Th_i^{4+} ions are available, interstitial Th_i^{4+} defect can form in ThO_2 with an energy release of 1.74 eV.

Comparatively for oxygen defects, the O^{2-} vacancy is the most possible one because of its smallest formation energy among oxygen defects. These two results reflect the ionic character of the Th-O bonds that each thorium atom almost loses 4 electrons to two oxygen atoms

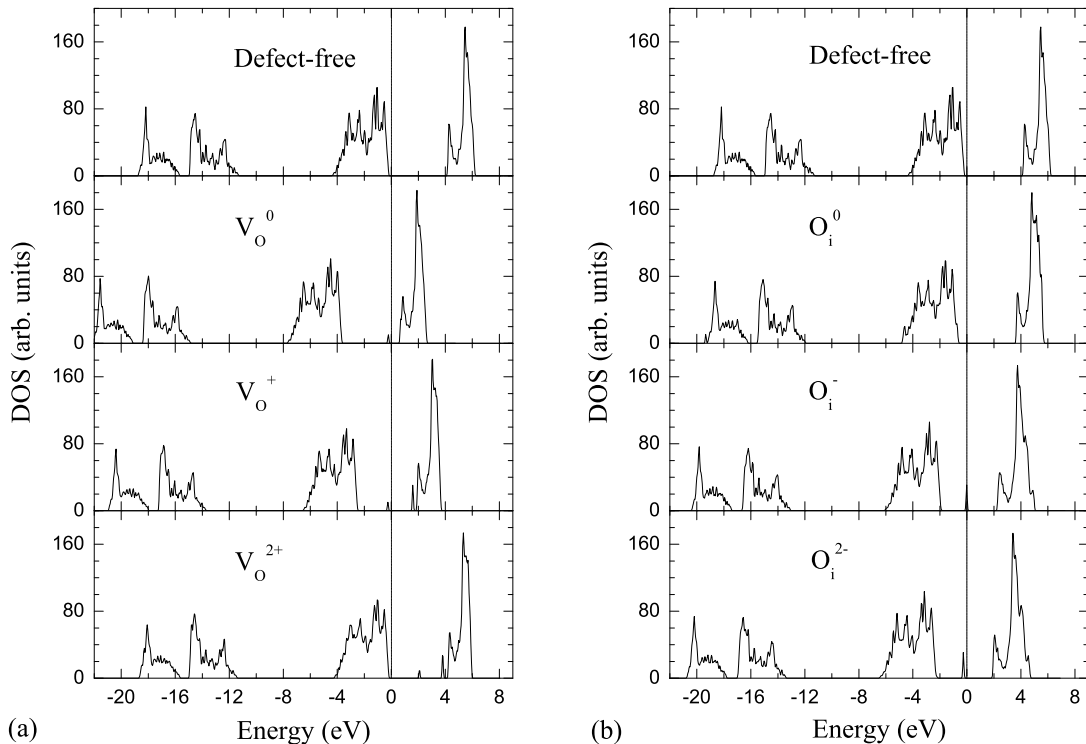


FIG. 8: (Color online) Electronic density of states (DOS) for ThO_2 with oxygen vacancies (a), and with interstitial oxygen defects (b) in different charge states. The Fermi energies are set to zero.

in ThO_2 . From Table I, we can also see that all thorium vacancies and thorium Frenkel-pairs have huge formation energies and thus can hardly form in intrinsic ThO_2 . Comparatively, the formation of oxygen Frenkel-pair, containing an O^{2+} vacancy and a interstitial O^{2-} ion has a relatively smaller formation energy.

Depending on the environment's influence on the Fermi energy of the ThO_2 material, the formation possibility of charged defects can change due to the changes on hardness of electrons transfer. Using Eqs. (7)-(9) under different Fermi energies, we can calculate the formation energy as a function of the Fermi energy for different kinds of defects. The corresponding results for oxygen (thorium) vacancies and interstitial oxygen (thorium) ions in different charge states are respectively shown in Figs. 7(a) and 7(b). The experimentally measured band-gap of 6.0 eV, instead of the 4.1 eV value obtained by first-principles calculations is chosen as the reference band-gap in discussions on defect formation.

As can be seen from Fig. 7(a), when comparing the energies associated with forming V_O^0 , V_O^+ , and V_O^{2+} oxygen vacancies, a transition can be observed with the Fermi level increasing from the valence band to the conduction band. The +2 charged oxygen vacancy is favored near the valence band, indicating that oxygen vacancies have a tendency to donate electrons or behave as a n -type defect. When the Fermi level increases to around 2.6 eV, the V_O^+ becomes energetically favorable. With further in-

creasing the Fermi level, the neutral charge state is most probable for oxygen vacancies, and the tendency of oxygen vacancy to donate electrons diminishes. We can also see from Fig. 7(a) that the interstitial O_i^{2-} defect can become very possible to form when the Fermi energy is shifted to be near the conduction band of ThO_2 .

From Fig. 7(b) we see that when the Fermi energy is near the valence band, all charged states of thorium vacancy are hard to form because of the huge formation energies, and the interstitial Th_i^{4+} ions can easily form in ThO_2 with a negative formation energy. With upshifting the Fermi energy, the interstitial thorium defect in neutral state and the V_Th^{4-} vacancy can both become the most possible thorium kinds of defects. When considering only the vacancy defects, V_O^{2+} is the most stable defect near the valence band, while near the conduction band, V_Th^{4-} is the most favorable one. Comparatively for interstitial states, the Th_i^{4+} and O_i^{2-} defects are the most probable ones when the Fermi energy is near the valence and conduction band respectively.

In addition, the electronic density of states (DOS) for both defect-free and defective ThO_2 are calculated and shown in Figs. 8 and 9, to further analyze the influences of the considered defects on the electronic structures of ThO_2 . As clearly shown in both Figs. 8 and 9, the introduction of vacancies or interstitial ions do not change the DOS distribution of ThO_2 very much. The biggest character in both Figs. 8 and 9 is that a new defect en-

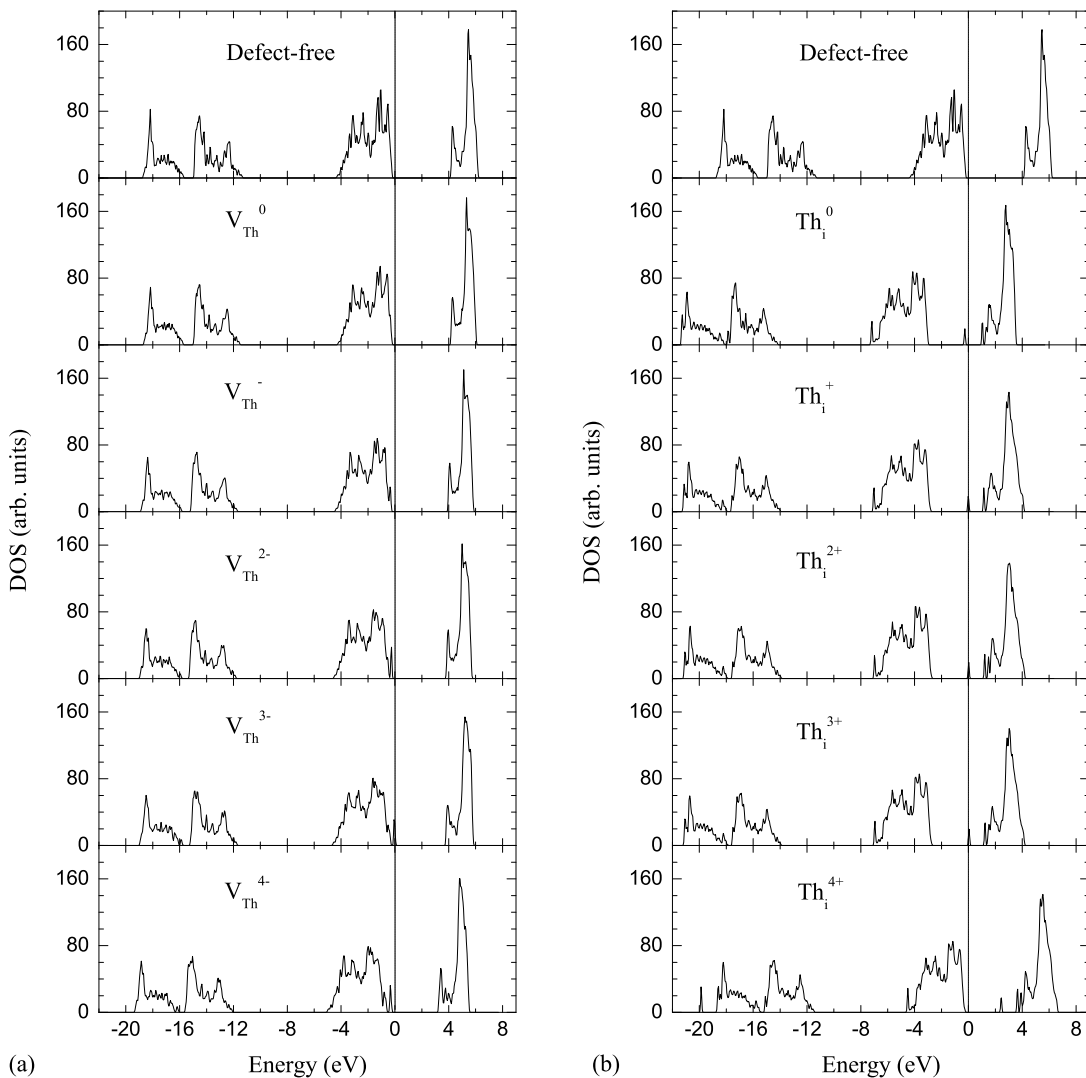


FIG. 9: (Color online) Electronic density of states (DOS) for ThO_2 with thorium vacancies (a), and with interstitial thorium defects (b) in different charge states. The Fermi energies are set to zero.

ergy level emerges in the band gap for defective ThO_2 . For the electronic structure of ThO_2 with oxygen vacancies, we see from Fig. 8(a) that the Fermi energy shifts from the valence band maximum (VBM) in defect-free ThO_2 , to above the defect energy level for the V_O^0 defect, and from above the defect energy level for the V_O^+ defect back to the VBM for the V_O^{2+} defect. For the system with interstitial oxygen ions, we can see from Fig. 8(b) that the Fermi energy shifts respectively from the VBM for the O_i^0 defect to the defect energy level for the O_i^- defect, and from the defect energy level for the O_i^- defect to above the defect energy level for the O_i^{2-} defect. Similarly for the ThO_2 supercell with interstitial thorium ions, the Fermi energy shifts from the VBM to the defect energy level for the Th_i^+ , Th_i^{2+} , and Th_i^{3+} defects, and then shifts to above the defect energy level for the Th_i^{4+} defect, as shown in Fig. 9(b). From Fig. 9(a), one can

see that the defect energy levels for thorium vacancies in ThO_2 are very close to the VBM.

E. Diffusion of helium in ThO_2

In order to determine the structure influence of helium impurity on ThO_2 , we systematically calculate the incorporation energy and diffusion energy barriers for helium in both the defect-free and defective ThO_2 . The incorporation energy is defined to be the energy required to incorporate one helium atom at a pre-existing vacancy or at an interstitial site. In this way, E_{inc} can be expressed as follows

$$E_{inc} = E_{tot} - E_{\text{ThO}_2} - E_{\text{He}}, \quad (14)$$

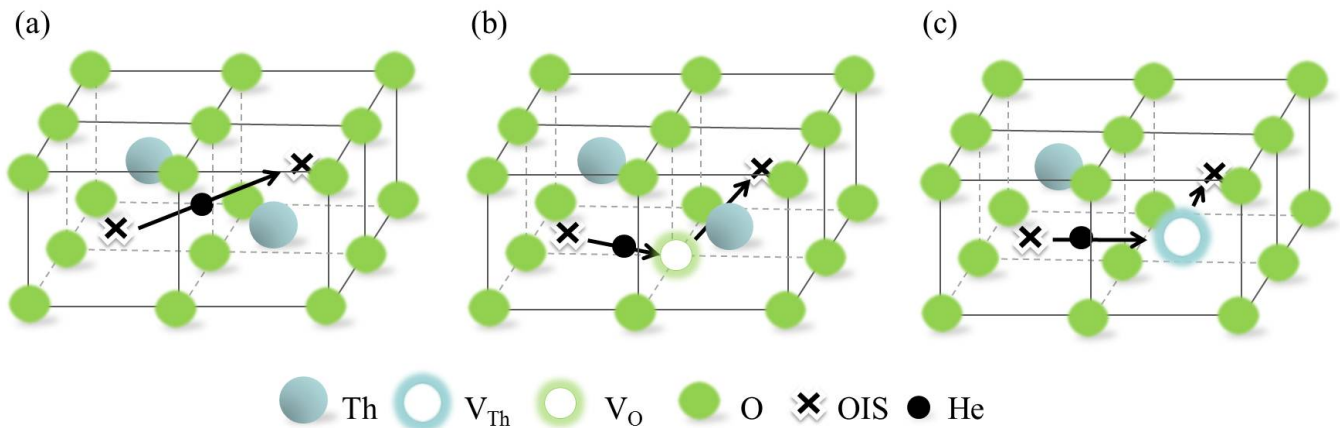


FIG. 10: (Color online) Diffusion pathways for a helium atom from one octahedral interstitial site to another octahedral interstitial site directly in intrinsic ThO_2 (a), through an oxygen vacancy (b) and through a thorium vacancy in defective ThO_2 (c).

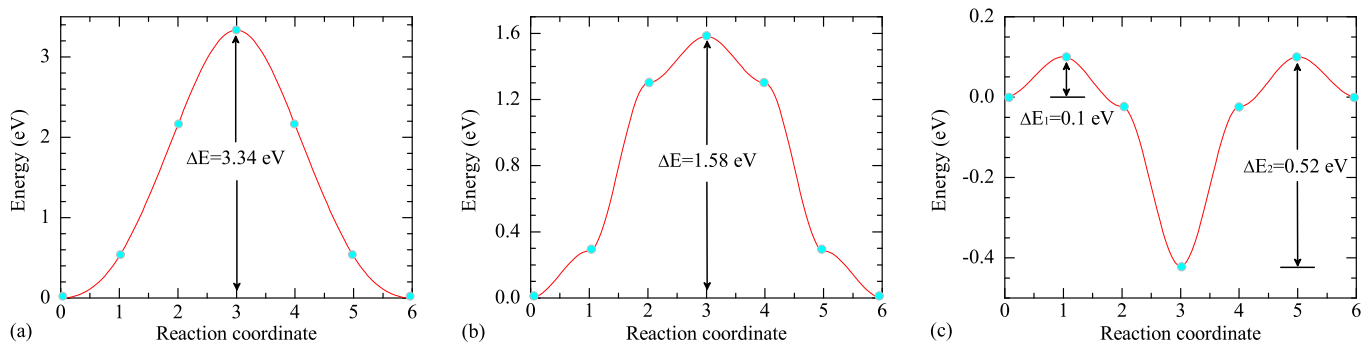


FIG. 11: (Color online) The energy profiles for a helium atom to diffuse from one octahedral interstitial site to another octahedral interstitial site directly in intrinsic ThO_2 (a), through an oxygen vacancy (b) and through a thorium vacancy in defective ThO_2 (c).

where E_{tot} is the energy of the ThO_2 supercell with an incorporated helium, E_{ThO_2} is the energy of the ThO_2 supercell with or without defects, and E_{He} the energy of an isolated helium atom. Three different kinds of incorporations are systematically considered here, i.e., a helium atom at the oxygen (O) and thorium (Th) sites in defective ThO_2 , and a helium atom at the octahedral interstitial site (OIS). The calculated incorporation energies are 2.48, 0.21, and 0.77 eV respectively. We can see that the most possible incorporation site for helium is the thorium vacancy site in defective ThO_2 . In comparison, the oxygen vacancy site is much less possible for helium incorporation.

The structural influence of helium on ThO_2 is determined not only by the incorporation energy, but also by the minimum energy path for helium diffusion. The climbing image nudged elastic band (CINEB) method [56] is then employed to find the minimum-energy diffusion pathways. Based on the obtained incorporation results for helium in ThO_2 , we here investigate the dif-

fusions of helium from OIS to OIS in both defect-free and defective ThO_2 . Figures 10(a)-(c) depict our considered diffusion ways. And the energy profiles along these paths are shown in Figs. 11(a)-(c) respectively. We can see from Fig. 11(a) that in intrinsic ThO_2 , the incorporated helium atom needs to overcome a 3.34 eV energy barrier in order to diffuse from one OIS to another. This huge diffusion energy barrier means that at normal temperatures, helium diffusion in intrinsic ThO_2 is almost impossible. In the corresponding saddle point along this diffusion path, the helium atom is at the middle of the two OISs, and the nearest oxygen atoms along the $[001]$ direction are repelled from each other by about 0.80 Å.

From the calculated energy profile shown in Fig. 11(b), we see that the energy barrier for an incorporated helium atom to diffuse from one OIS to another by passing an oxygen vacancy is lowered down to be 1.58 eV. This energy barrier is however still too large for the diffusion to happen at room temperatures. The only possible way for helium to diffuse in ThO_2 is found to be passing through

a thorium vacancy, as depicted in Fig. 10(c). We can see from Fig. 11(c) that the helium atom only needs to overcome a 0.10 eV energy barrier to diffuse from an OIS to the thorium vacancy, and a 0.52 eV energy barrier to diffuse from the thorium vacancy to another OIS. The small energy barriers for helium to diffuse in thorium vacancy-included ThO₂ indicate that thorium vacancies might lead to helium aggregation causing failure of the ThO₂ material. Fortunately from our above defect formation studies, the formation of thorium vacancies is almost forbidden when the Fermi energy is not upshifted, because of their too large formation energy in ThO₂. Therefore, to keep ThO₂ away from structural damages from helium incorporation, any kinds of factors possibly leading to upshifts of the Fermi energy should be avoided.

IV. SUMMARY

In summary, we have performed a systematic first-principles study to investigate the thermodynamic properties and structural stabilities of ThO₂. Based on the calculated phonon dispersion curves for ThO₂, we systematically analyze its thermodynamic properties and obtain the values of its thermal expansion coefficient, bulk modulus, and heat capacities at different temperatures, which are in good agreement with corresponding experimental measurements. The agreement between our calculations and experiments also proves the validity of our methods and model, and the effectiveness of the quasi-harmonic approximation. According to the Umklapp interaction mechanism between different phonon

branches, we systematically obtain the mode Grüneisen parameters, and further calculate the thermal conductivities of ThO₂. Within the temperature range from Debye temperature to about 1500 K, our calculated thermal conductivity accords very well with experimental results.

In addition to studying the thermodynamic properties of ThO₂, we also investigate its structural stability by calculating the formation energy of different defects, and the diffusion behaviors of helium, during which different charge states of the defects are considered. The formation energy results indicate that without any shifts of the Fermi energy, the interstitial Th⁴⁺ defect is very probable to appear in ThO₂ with an energy release of 1.74 eV. With changing the Fermi energy to different values, the formation possibilities of different defects varies. For helium incorporation, it is found that the helium atom tends to occupy a thorium vacancy in defective ThO₂ or occupy the octahedral interstitial site in intrinsic ThO₂. It is further revealed that incorporated helium atoms can only diffuse freely in the thorium-vacancy contained ThO₂, with small energy barriers of 0.10 and 0.52 eV. Our studies point out that to avoid helium damage, the electronic Fermi energy of ThO₂ should not be upshifted because it can makes the formation of thorium vacancies less possible.

V. ACKNOWLEDGMENTS

This work was supported by NSFC under Grant No. 51071032, and by Foundations for Development of Science and Technology of China Academy of Engineering Physics under Grants No. 2011A0301016 and No. 2011B0301060.

-
- [1] J. Belle, *J. Nucl. Mater.* **30**, 3 (1969).
 - [2] J. C. Killeen, *J. Nucl. Mater.* **88**, 185 (1980).
 - [3] K. N. Kudin, G. E. Scuseria, and R. L. Martin, *Phys. Rev. Lett.* **89**, 266402 (2002).
 - [4] B. Dorado, B. Amadon, M. Freyss, and M. Bertolus, *Phys. Rev. B* **79**, 235125 (2009).
 - [5] B. Dorado, G. Jomard, M. Freyss, and M. Bertolus, *Phys. Rev. B* **82**, 035114 (2010).
 - [6] L. Petit, A. Svane, Z. Szotek, W. M. Temmerman, and G. M. Stocks, *Phys. Rev. B* **81**, 045108 (2010).
 - [7] J. S. Herring, P. E. MacDonald, K. D. Weaver, C. Kullberg, *Nucl. Eng. Des.* **203**, 65-85 (2001).
 - [8] J. Tommasi, A. Puill, and Y.K. Lee, "Reactors with Th/Pu Fuels," Proc. Workshop Advanced Reactors with Innovative Fuels, Villigen, Switzerland, October 21-23 (1998).
 - [9] R. Maitura, *Nucl. Rep.* 46-53 (2005).
 - [10] H. Chang, Y. Yang, X. Jing, and Y. Xu, "Thorium-Based Fuel Cycles in the Modular High Temperature Reactor," *Tsinghua Sci. Tech.* **11**, 6 (2006).
 - [11] A. Carrera, J. Lacouture, C. Campo, and G. Paredes, "Feasibility Study of Boiling Water Reactor Core Based on Thorium-Uranium Fuel Concept," *Energy Conversion Management*, **49**, 1 (2007).
 - [12] P. E. Juhn, "Thorium Fuel Cycle Options for Advanced Reactors: Overview of IAEA Activities," Proc. Workshop Advanced Reactors with Innovative Fuels, Villigen, Switzerland, October 21-23 (1998).
 - [13] A. C. Momin and Karkhanvala, *High Temp. Sci.* **10**, 45 (1978).
 - [14] J. R. Springer, E. A. Eldridge, M. U. Goodyear, T. R. Wright and J. F. Lagedrast Report No. BMI-X-10210 (1968).
 - [15] J. C. Weilbacher, *High Temp.-High Press.* **4**, 431 (1972).
 - [16] D. L. McElroy, J. P. Moore, P. H. Spindler, Oak Ridge National Laboratory Report ORNL-4429, p. 121 (1968).
 - [17] Armour Research Foundation ARF-Project No. 6-025, Final Report, (1957).
 - [18] M. Murabayashi, *J. Nucl. Sci. Technol.* **7**, 559 (1970).
 - [19] C. G. S. Pillai, P. Raj, *J. Nucl. Mater.* **277**, 116-119 (2000)
 - [20] W. G. Bradshaw, C. O. Mathews, Report LMSD-2466, (1958).
 - [21] J. P. Moore, R. S. Graves, T. G. Kollie, D. L. McElroy, Oak Ridge National Laboratory Report ORNL-4121, (1967).

- [22] P. Srirama Mufti, C. K. Mathews, *J. Phys. D* **24**, 2202 (1991).
- [23] K. Bakker, E. H. P. Corfunke, R. J. M. Konings and R. P. C. Scharm, *J. Nucl. Mater.* **250**, 1-12 (1997).
- [24] D. Chadwick and J. Graham, *Nat. Phys. Sci.* **237**, 127 (1972).
- [25] G. C. Allen and P. M. Tucker, *J. Chem. Soc. Dalton* p. 470 (1973).
- [26] B. W. Veal and D. J. Lam, *Phys. Rev. B* **10**, 12 (1974).
- [27] A. Jayaraman, G. A. Kourouklis, L. G. Van Uitert, *Pramana* **30**, 225 (1988).
- [28] J. P. Dancausse, E. Gering, S. Heathman, U. Benedict, *High Pressure Res.* **2**, 381 (1990).
- [29] M. Idiri, T. Le Bihan, S. Heathman, J. Rebizant, *Phys. Rev. B* **70**, 014113 (2004).
- [30] Y. -E. Kim, J. -W. Park and J. Cleveland, "Thermophysical properties database of materials for light water reactors and heavy water reactors", Vienna, (2006).
- [31] C. Sevik and T. Cagin, *Phys. Rev. B* **80**, 014108 (2009).
- [32] V. Kanchana, G. Vaitheeswaran, A. Svane, A. Delin, *J. Phys.: Condens. Matter* **18**, 9615 (2006).
- [33] I. R. Shein, K. I. Shein, A. L. Ivanovskii, *J. Nucl. Mater.* **361**, 69 (2007).
- [34] J. C. Boettger, *Int. J. Quantum. Chem.* **109**, 3564 (2009).
- [35] B. T. Wang, H. L. Shi , W. D. Li , P. Zhang, *J. Nucl. Mater.* **399**, 181-188 (2010).
- [36] A. Boudjemline, L. Louail, Mazharul M. Islam, B. Diawara, *Comp. Mater. Sci.* **50**, 2280-2286 (2011).
- [37] G. Kresse, J. Furthmüller, computer code VASP, Vienna, (2005).
- [38] G. Kresse, J. Furthmüller, *Phys. Rev. B* **54**, 11169 (1996).
- [39] P. E. Blöchl, *Phys. Rev. B* **50**, 17953 (1994).
- [40] J. P. Perdew, K. Burke, M. Ernzerhof, *Phys. Rev. Lett.* **77**, 3865 (1996).
- [41] H. J. Monkhorst, J. D. Pack, *Phys. Rev. B* **13**, 5188 (1976).
- [42] A. Baldereschi, S. Baroni, R. Resta, *Phys. Rev. Lett.* **61**, 734 (1988).
- [43] M. Peressi, N. Binggeli, A. Baldereschi, *J. Phys. D* **31**, 1273 (1998).
- [44] F. Brich, *Phys. Rev.* **71**, 809 (1947).
- [45] J. S. Olsen, L. Gerward, V. Kanchana, G. Vaitheeswaran, *J. Alloys Compd.* **381**, 37 (2004).
- [46] Y. Lu, D. F. Li, R. W. Li, H. L. Shi, P. Zhang, *J. Nucl. Mater.* **408**, 136-141 (2011).
- [47] P. Zhang, B. T. Wang, and X. G. Zhao, *Phys. Rev. B* **82**, 144110 (2010).
- [48] P. M. Macedo, W. Capps, J. B. Watchman, *J. Am. Ceram. Soc.* **47**, 651 (1964).
- [49] Y. S. Touloukian, R. K. Kirby, R. E. Taylor, T. Y. R. Lee, *Thermal Expansion. Nonmetallic Solids (IFI/Plenum, New York, 1970).*
- [50] G. A. Slack, *J. Phys. Chem. Solids* **34**, 321 (1973).
- [51] G. A. Slack, *Solid State Phys.* **34**, 1 (1979).
- [52] O. L. Anderson, *J. Phys. Chem. Solids* **12**, 41 (1959).
- [53] A. A. Blanco, E. Francisco, and V. Luana, *Comput. Phys. Commun.* **158**, 57 (2004).
- [54] E. Francisco, J. M. Recio, M. A. Blanco, A. Martín Pendás, *J. Phys. Chem.* **102**, 1595 (1998).
- [55] E. Francisco, M. A. Blanco, and G. Sanjurjo, *Phys. Rev. B* **63**, 094107 (2001).
- [56] G. Henkelman, B. P. Uberuaga, and H. Jonsson, *J. Chem. Phys.* **113**, 9901 (2000).